Intrinsic Magnetism of Grain Boundaries in Two-Dimensional Metal Dichalcogenides

Zhuhua Zhang,[†] Xiaolong Zou,[†] Vincent H. Crespi,[‡] and Boris I. Yakobson[†,*]

[†]Department of Mechanical Engineering and Materials Science, Department of Chemistry, and the Smalley Institute for Nanoscale Science and Technology, Rice University, Houston, Texas 77005, United States and [‡]Department of Physics and Materials Research Institute, The Pennsylvania State University, University Park, Pennsylvania 16802-6300, United States

ABSTRACT Grain boundaries (GBs) are structural imperfections that typically degrade the performance of materials. Here we show that dislocations and GBs in two-dimensional (2D) metal dichalcogenides MX_2 (M = Mo, W; X = S, Se) can actually *improve* the material by giving it a qualitatively new physical property: magnetism. The dislocations studied all display a substantial magnetic moment of ~1 Bohr magneton. In contrast, dislocations in other well-studied 2D materials are typically nonmagnetic. GBs composed of pentagon–heptagon pairs interact ferromagnetically and transition from semiconductor to half-metal or metal as a function of tilt angle and/or doping level. When the tilt angle exceeds 47°, the structural energetics favor square–octagon pairs and the GB becomes an antiferromagnetic semiconductor. These exceptional magnetic properties arise from interplay of dislocation-induced localized states, doping, and locally unbalanced stoichiometry. Purposeful engineering of topological GBs may be able to convert MX_2 into a promising 2D magnetic semiconductor.

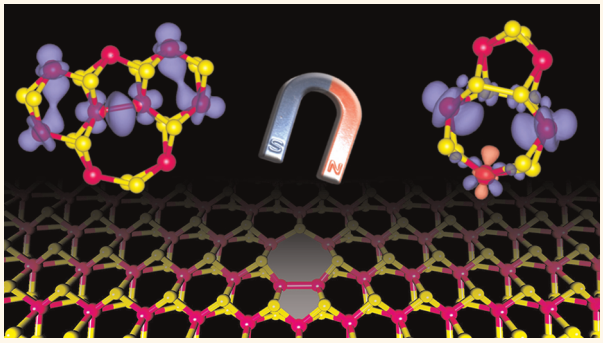

KEYWORDS: metal dichalcogenide · dislocation · grain boundary · magnetism · two-dimensional material

Nanostructured magnetic semiconductors have attracted extensive attention,[1,2] since they could enable the simultaneous control of spin and charge, promising enhanced efficiency for electronic devices and enriching them with new functions. Following the advent of graphene, there has been an upsurge of interest in the intrinsic magnetism in two-dimensional (2D) crystals. While experiments have detected ferromagnetic signals in certain graphene samples,[3−7] these systems show some significant limitations.[8] First, the vanishing band gap of graphene is undesirable for switching functionalities and certain mechanisms of controllable magnetism. Second, magnetism in graphene appears to originate from vacancies,[9−12] adatoms,[13−18] or zigzag edges,[19−21] imperfections that can be readily removed by local structural rearrangements through annealing or chemical passivation.[22] Global topological defects such as dislocations within grain boundaries (GBs) are more robust, since they cannot be annealed away by a purely local structural rearrangement. GBs are ubiquitous in 2D materials, forming at the interstices of distinct grains that nucleate during growth;[23−27] in the case of graphene[27−30] and heteroelemental hexagonal boron nitride (h-BN),[31,32] GBs are stable strings of pentagon–heptagon (5|7) dislocations. However, in these materials they are established to be nonmagnetic.

In contrast, here we discover that the grain boundaries in inorganic analogues of graphene, single-layer transition metal dichalcogenides MX_2 (M = Mo, W; X = S, Se), are magnetic. These newly emerged 2D materials of prominent current interest have an intrinsic band gap of 1.4 to 2.0 eV and are superior to graphene in certain respects.[33−40] Unlike graphene, the 2D MX_2 family has metal–ligand bonding and a three-atom thickness, with the M atoms sandwiched between layers of X ligands in a trigonal prismatic geometry. The crystal field splitting of M orbitals combined with reduced dimensionality in single-layered MX_2 yields a direct band gap.[37,38] Like all crystalline materials, these MX_2 are prone to polycrystallinity,[41]

* Address correspondence to biy@rice.edu.

Received for review October 10, 2013 and accepted November 10, 2013.

Published online November 11, 2013
10.1021/nn4052887

and recent experiments reveal a variety of dislocations and GBs in MoS_2 samples.[42−46] Unlike in graphene or h-BN, dislocations in MX_2 have a finite thickness, forming dreidel-shaped polyhedra.[41,47] Little from the extensive study of GBs in graphene[24−30] can be generalized to the MX_2 family, where qualitatively new phenomena can be anticipated.

Below we show by first-principles calculations that dislocation cores in 2D MX_2 can possess substantial magnetism, resulting from partial occupancy of spin-resolved localized electronic states, with significant spin−spin interactions when the dislocations are aligned into a GB. The magnetic energy, spin ordering, and electronic properties of GBs strongly depend on the GB tilt angle, the type of constituent dislocations, and the doping level. Grain boundaries composed of 5|7 rings behave as a ferromagnetic half-metallic nanowire in a range of moderate tilt, while grain boundaries composed of 4|8 cores form antiferromagnetic semiconductors. These results uncover an interesting interplay between dislocation morphology, doping, and the spin degrees of freedom and open new avenues for exploring spintronics in semiconducting MX_2.

Detailed calculation methods and models are provided in the Methods section. To establish the generality of the results, we implement grain boundaries and dislocations within three distinct structural models: a MX_2 nanoribbon containing a single GB connecting two tilted domains; an extended model with periodic boundary conditions containing a pair of complementary GBs, and a GB loop model (embedded in periodic boundary conditions) with three Mo-rich dislocations (see Figures S1 and S2a in the Supporting Information). These models isolate and control for the effects of nanoribbon edges and GB dipoles; the ubiquity of magnetism across all three gives confidence in the conclusions.

RESULTS AND DISCUSSION

In projection to the basal plane, the MX_2 sheet is isomorphic to graphene or h-BN, with the M atom in one sublattice and superimposed X's in the other (Figure 1a). A dislocation thus can be created in MX_2 by following the same procedure as in graphene:[48] for example, removing half of an armchair atomic line and reconnecting seamlessly all of the resultant dangling bonds yields a 5|7 core. The strain energy is proportional to the square of the Burges vector $|\mathbf{b}|^2$; this is lowest for the 5|7 core. In contrast to graphene, bielemental MX_2 has two types of 5|7 dislocations: an M-rich dislocation with an M−M bond and $\mathbf{b} = (1,0)$, which we call ⊥, and an X-rich dislocation we call ⊤ with an X−X bond and $\mathbf{b} = (0,1)$. Energetically unfavorable homoelemental bonds can be avoided by using a 4|8 core (created by removing two parallel zigzag atomic chains). However, this dislocation has a $\sqrt{3}$-times larger Burgers vector $\mathbf{b} = (1,1)$. The larger strain energy $\sim|\mathbf{b}|^2$ makes an isolated 4|8 dislocation unlikely, although they can become favorable when compactly aligned in a high-tilt GB, as discussed later.

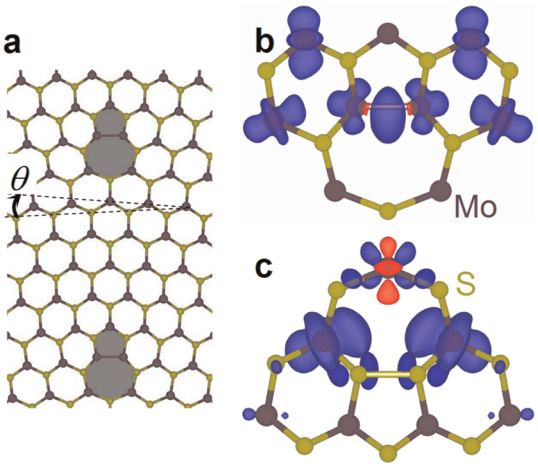

Figure 1. Structure of grain boundary in single-layer MoS_2. (a) Symmetric GB with a tilt angle $\theta = 9°$. Each repeat cell includes a Mo-rich ⊥ with a homoelemental Mo−Mo bond, tagged as Mo-rich ⊥. Reversing the grain tilt to $-9°$ creates a S-rich ⊤ with two S−S bonds. Isosurface plots (2×10^{-3} e/Å^3) show the magnetization densities of (b) Mo-rich ⊥ and (c) S-rich ⊤. Blue and red colors denote positive and negative values of the magnetization density, respectively.

Considering that most experimental work on GBs in MX_2 studies MoS_2, we mainly focus on this material and consider the other MX_2 compositions later (see Figure S7; they show similar properties). Figure 1b and c present the ground-state magnetization densities of isolated Mo-rich ⊥ and S-rich ⊤ dislocations, as extracted from the ribbon model (the periodic model shows a similar spin splitting and level ordering). This system is actually a low-tilt 9° GB, but at this low dislocation density the defects are well separated. The spin polarization is highly localized at the dislocations, embedded within an ambient 2D semiconducting host. In the Mo-rich ⊥ the spin is mainly on the Mo−Mo bond and its four nearest-neighbor Mo atoms. In the S-rich ⊤ the spin sits mostly on the three Mo atoms of the heptagon, particularly on the two atoms adjacent to the S−S pair. Both dislocation types have total magnetic moments of $\mu = 1.0\ \mu_B$ (calculations with hybrid functionals confirm these results as well; see Figure S2). The energy difference between nonmagnetic and magnetic states is substantial: ∼36 meV per dislocation. Magnetism intrinsic to dislocations has not been reported previously, to our knowledge, in any 2D material. Magnetism of dislocations, as robust defects imbedded in the 2D material, is novel and distinctly different from magnetic edge states along bare zigzag edges[49−52] or at some special vacancies[53] with their volatile structures and even composition sensitive to environment conditions.

Dislocations are natural constituents of grain boundaries and thus should endow magnetism to them. Here, we consider symmetric GB lines bisecting the tilt angle θ between adjacent grains, as in Figures 1a and S1

in the Supporting Information. A non-bisector GB has higher strain energy than a symmetric one; although not discussed here, they can also be magnetic. Figure 2a shows the GB's magnetic moment per unit length M as a function of the tilt angle θ, with proportionality evident below $\theta = 32°$. The linear density of dislocations in low-angle GBs is $2\sin(\theta/2)/b \approx \theta/b$;[54] thus the linear moment density is proportional to the tilt angle: $M \approx \mu\theta/b$, where μ is the moment of each dislocation. Interestingly, the Mo-rich GBs sustain this proportionality up to a larger tilt angle than do the S-rich GBs: the local moments of the S-rich ⊤ decrease as the S−S bonding geometry becomes more distorted at higher θ (this distortion may also help explain why S-rich GBs have not yet been found experimentally).

Above 32° the number of 5|7 dislocations declines and hexagons with homoelemental bonds appear instead (symmetric "s-hexagons"). As shown in Figure 2a, GBs with s-hexagons support further increase in the magnetic moment up to about $\theta = 47°$, but at higher angles the magnetism collapses as the GB approaches a state of pure s-hexagons at $\theta = 60°$. At $\theta = 47°$, we obtain $M = 1.75\ \mu_B$/nm for the Mo-rich GB and $M = 1.55\ \mu_B$/nm for the S-rich GB. These values are significantly higher than the spin density of 1.2 μ_B/nm calculated for zigzag graphene edges. The precise magnetization densities attained in experimental systems will be sensitive to the doping level, as discussed below.

As depicted in Figure 2b, above $\theta = 47°$ the 4|8 core becomes more favorable than the 5|7 core: although it has a larger Burgers vector, it has no homoelemental bonds. The prevalence of 8-fold rings at high tilt angles is consistent with recent experimental data on grain boundary structures.[42−44] At $\theta = 60°$ the cancellation of stress fields between adjacent 4|8s lowers the GB energy by ∼3.2 eV/nm from that of an array of homoelemental bonds (*i.e.*, all s-hexagons). In contrast, for graphene and h-BN the 5|7s plus hexagons are always preferred over 4|8s. As shown in Figure 2a, the magnetic moment of these 4|8 GBs sharply increases as one approaches 60°, reaching 2.1 μ_B/nm in magnitude, which is higher than the maximum achieved by 5|7 boundaries; the spin-polarization energy reaches 45 meV per dislocation. (We quote the magnitudes of local moments which are similar for ferro- and antiferromagnetic states.) 4|8s can also appear in antisymmetric zigzag GBs (invariant to mirror reflection with element inversion). A recently observed GB composed of 8|4|4|8 units[42] that is slanted by 11° from the antisymmetric 60° zigzag GB reaches $M = 1.2\ \mu_B$/nm (see Figure S4). At high tilt, the strongly magnetic 4|8 and 8|4|4|8 structures surpass the 5|7 dislocations.

What is the strength of the spin coupling? We compare the energies of GBs with ferromagnetic (FM) or antiferromagnetic (AFM) order between adjacent dislocations. In GBs composed of 5|7s, the FM structure

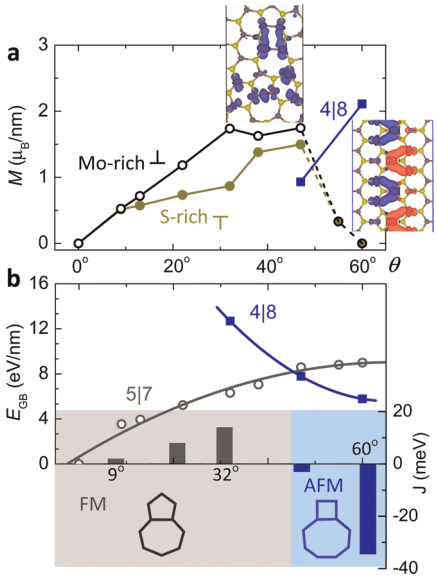

Figure 2. Tilt-dependent magnetism of GBs in MoS_2. (a) Magnetic moment M per unit length of GB as a function of tilt angle. All values are obtained from GBs with FM order. Insets show magnetization densities (isovalue 2×10^{-3} e/Å^3) of a 38° GB composed of Mo-rich ⊥ and a 60° GB composed of 4|8s. (b) Top left axis: energies of GBs as a function of θ, with gray circles for GBs composed of 5|7s and blue squares for GBs composed of 4|8s. Bottom right axis: exchange coupling parameter J for several typical GBs composed of Mo-rich ⊥ or 4|8s.

is energetically preferred. For the Mo-rich grain boundary, $E_{AFM} - E_{FM}$ is ∼8 meV for $\theta = 22°$ and increases to ∼14 meV for the more closely spaced dislocations at $\theta = 32°$. In contrast, grain boundaries with 4|8 cores favor an AFM structure: at $\theta = 60°$ we obtain $E_{AFM} - E_{FM} \approx -32$ meV. This distinction may be related to carrier-mediated ferromagnetism:[55] the 5|7 defects support free charge carriers at these doping levels, whereas the 4|8 defects do not, as shown in Figure 4. Another important distinction between the 5|7 and 4|8 cases is homoelemental bonds in the former but not the latter. Mapping these DFT-computed energies onto a 1D nearest-neighbor Ising model $H = -J\sum_i \mathbf{S}_i\mathbf{S}_{i+1}$ where J is the spin−spin interaction and $\mathbf{S}_i$ is the spin of the ith dislocation (with $S = 1/2$), we obtain J as a function of θ in Figure 2b. For GBs containing 5|7 dislocations, J is positive and increases as the separation between dislocations decreases at larger tilt angle. GBs composed of 4|8s have negative J, again larger in magnitude for higher tilt angles. For the most strongly interacting local moments, at $\theta = 32°$ for FM ordering and $\theta = 60°$ for AFM ordering, the characteristic energy scale for spin fluctuations is on the order of room temperature in the AFM case and a significant fraction thereof for the FM case. However, long-ranged magnetic order is not anticipated unless further spin couplings can be introduced to increase the effective dimensionality. Spin-orbit interactions should also impose crystalline anisotropy onto these spins, a topic for future investigation.

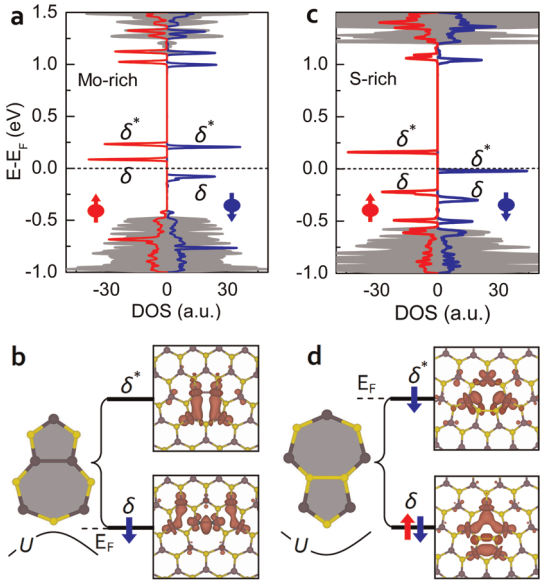

Figure 3. Electronic structure analyses of dislocations in MoS_2. (a) Spin-polarized density of states (DOS) of a 9° GB composed of Mo-rich ⊥. Solid lines are the DOS projected onto those atoms forming the GB, while gray-shaded regions are the DOS projected onto atoms in bulk area. (b) Schematic energy levels of ⊥-induced spin-unresolved localized states, δ and δ*, and their corresponding isosurface (5×10^{-4} e/Å^3) distributions of partial charge densities. A local potential maximum around the ⊥ is illustrated by a potential profile. (c, d) Corresponding cases for a 9° GB composed of S-rich ⊤, showing a local potential minimum. The single arrow denotes a partially occupied energy level.

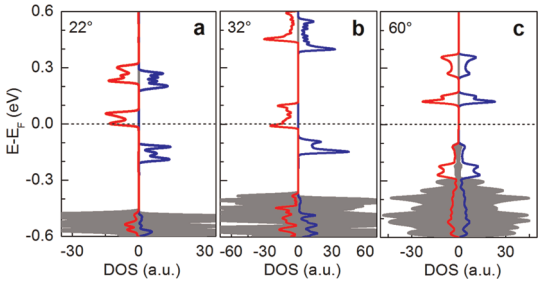

Figure 4. Tilt-dependent ground-state electronic properties of GBs in MoS_2. Spin-polarized DOS of (a) 22° and (b) 32° GBs composed of Mo-rich ⊥ as well as (c) a 60° GB composed of 4|8s. The color stipulations are the same as in Figure 3a.

To understand better why dislocations and grain boundaries in MoS_2 are magnetic, we examine their electronic structure. Figure 3a shows the spin-polarized density of states of the 9° GB described earlier, projected onto just the atoms of the Mo-rich dislocation, compared to that of an ideal defect-free MoS_2, shown in gray. Two new localized states—predominately Mo $4d_{x^2-y^2,xy}$ and $4d_{z^2}$ with a small admixture of S $3p_x$—appear within the bulk band gap, marked by δ and δ*. The δ state has bonding character around the Mo−Mo bond, while the δ* has antibonding character, as shown in Figure 3b. The local excess of Mo weakens the crystal potential slightly, elevating these states slightly in energy relative to the dislocations in the S-rich GB; see Figure S3. At an appropriate doping level, these localized states become partially occupied; within a simple Stoner model, when the δ state crosses the Fermi level, the density of states could trigger spontaneous spin splitting. The spin polarization of the Mo-rich ⊥ thus echoes the spatial distribution of the δ state, comparing Figures 1b and 3b. If two S atoms were inserted into the Mo−Mo bond of the Mo-rich ⊥ to balance the local excess of Mo, the resultant 6|8 dislocation would be nonmagnetic.

Since grain boundaries comprise a small fraction of a typical experimental 2D system, these dislocation-induced midgap states will have a low overall areal density. Thus, the precise location of the Fermi level relative to these mid-gap states will be a sensitive function of the doping conditions. In the calculations, the system is self-doped by the unterminated ribbon edges in the nanoribbon model or by band overlap between complementary dislocations of opposite character in the periodic model. The GB loop model, in contrast, has three identical dislocations and no edge effects: the appearance of magnetism in this system demonstrates that self-doping through band overlap is not required for magnetism. Experiment will provide more fine-grained control of the doping level, through external gating or intrinsic chemical doping. Thus the calculations presented here should be looked upon as a detailed explication of the magnetic response for one particular choice of Fermi energy; calculations (Figure S5) of the magnetic properties as a function of doping level (with jellium background) reveal the anticipated tunable magnetic response.

A similar analysis applies for the S-rich ⊤, except with a slight downward shift to the defect states and a spin-polarized antibonding δ* state, as shown in Figure 3c and d. Alleviating the S-excess in the ⊤ by removing two S atoms results in nonmagnetic 4|6 dislocation. The GB composed of 4|8s also lacks homoelemental bonds. However, it does support a magnetic state, albeit one with antiferromagnetic alignment of spins on adjacent dislocations and no net overall spin polarization. The spin polarization again mainly resides on Mo atoms, as shown in the right inset of Figure 2a. The Mo−Mo distance is reduced within the GB, compared to that in the bulk-like region.

Can the magnetic grain boundaries in MoS_2 be half-metallic? With increasing tilt angle the overlap between the electronic states on adjacent dislocations is large; this not only increases the exchange coupling but also broadens the states into dispersive bands. If the defect band for just one spin channel crosses the Fermi level, we obtain a half-metal. Figure 4a and b present spin-polarized density of states for the Mo-rich GBs of 22° and 32° tilt within the ribbon model. The spin splitting is larger than the bandwidth, so both systems can support a gap in the spin-down channel with a metallic spin-up channel. Charge transport along the GBs is thus fully spin-polarized. Both the ribbon and the periodic models exhibit half-metallic behavior in the range $13° < \theta \leq 32°$ (see Figure S6).

The two models show slight differences in the Fermi level placement due to different self-doping conditions; in experiment, this doping level will be gate-controllable. Below this tilt range, the GB is a magnetic semiconductor within our models (*e.g.*, the 9° GB of Figure 3), since the band dispersion along the GB is too small to metalize any spin channel under our self-doping conditions. Above $\theta = 32°$, states associated with s-hexagons become important and the half-metallic nature is not consistently maintained. At $\theta = 60°$, GBs composed of 4|8s are antiferromagnetic semiconductors with a band gap of 0.2 eV, as shown in Figure 4c. These results promise that purposeful engineering of topological GBs can tailor spin-dependent transport in 2D MoS_2.

The semiconducting bulk state of MoS_2 provides the appropriate electronic environment, and the transition metal−ligand bonds then provide the local chemistry necessary to induce magnetism at grain boundaries of MoS_2. Magnetic GBs are thus common within this family of transition metal dichalcogenides, including WS_2, $MoSe_2$, and WSe_2 (Figure S7). In contrast, GBs in π-bonded graphene and h-BN or metallic 1T MX_2 are nonmagnetic (see Figure S8 and related discussions in the Supporting Information). Very recently, Wang *et al.* developed a method by transmitted electrons to determine atomic site-specific magnetic structure on a nanometre scale,[56] which may open the door to detecting the magnetism at dislocations in MoS_2.

CONCLUSIONS

In summary, a comprehensive analysis including first-principles calculations focused on the spatial distribution of spin polarization in states localized to the grain boundaries reveals intrinsic magnetism for dislocations and grain boundaries in metal dichalcogenides. The dislocations possess a substantial, doping-dependent magnetic moment associated with localized defect states centered on Mo 4d orbitals within the band gap of pristine MoS_2. GBs composed of 5|7 dislocations show ferromagnetic spin ordering, which varies from semiconductor to half-metal to metal depending on the intergrain tilt angle and doping level. At the largest tilts, grain boundaries containing 4|8 dislocations are favored; these are antiferromagnetic semiconductors. The semiconducting nature of MX_2, its unique 2D metal−ligand bonding, and the local homopolar bonding within dislocations are apparently the principal factors governing this unusual magnetic behavior. Grain boundaries are ubiquitous in 2D materials. This coupling of spin and dislocations opens a new avenue toward developing 2D magnetic semiconductors through grain boundary engineering.

METHODS: COMPUTATIONAL DETAILS

Calculations were mainly performed with the Vienna Ab-initio Simulation Package (VASP),[57,58] using the projector-augmented wave method[59] for the core region and spin-polarized density functional theory (DFT) based on the generalized gradient approximation (GGA) of Perdew−Burke−Ernzerhof[60] with a plane-wave kinetic energy cutoff of 350 eV. A vacuum layer of 16 Å isolates neighboring periodic images, and the Brillouin zone is sampled by 12 *k*-points. All atomic positions are relaxed using conjugate-gradient techniques until the force on each atom is less than 0.01 eV/Å. Additional tests using the GGA+*U* method ($U = 4$ and 2 eV for Mo and S, with corresponding J being 0.3 and 0.1 eV, respectively) as well as extensive computations with the hybrid functional developed by Heyd, Scuseria, and Ernzerhof (HSE06[61]) yielded similar results on magnetism, with an even stronger local moment than that obtained within pure GGA. For simplicity, the nanoribbon edges are unterminated: the actual experimental reconstruction of a MoS_2 edge is a complex question that can be circumvented for our purposes by using a wide-enough ribbon to isolate the GB from the edge (Figure S1a) and projecting the density of states onto just those atoms in the immediate vicinity of the GB; questions of self-doping from edge to GB are fully addressed when discussing the electronic properties of grain boundaries. A single dislocation is modeled by a GB with a minimal tilt of 9°, so that the dislocations are well spaced by ~2 nm (Figure 1a).

Conflict of Interest: The authors declare no competing financial interest.

Acknowledgment. The authors thank Andriy Nevidomskyy for useful discussions. This work was supported by the U.S. Army Research Office MURI grant W911NF-11-1-0362, and in part by the Robert Welch Foundation (C-1590). The computations were performed at the Data Analysis and Visualization Cyberinfrastructure funded by NSF grant OCI-0959097 to Ken Kennedy Institute.

Supporting Information Available: Structural models of GBs, magnetization density of a GB loop and that of Mo-rich 5|7 dislocation by HSE06 calculations, local electrostatic potential around the dislocations, magnetization density for a GB composed of 8|4|4|8 dislocations, carrier-tunable magnetism in different dislocations, half-metallic nature in the GBs constructed by 2D periodic model, and magnetization densities of 22° GBs in other 2D MX_2 compositions are collected. This material is available free of charge *via* the Internet at http://pubs.acs.org.

REFERENCES AND NOTES

1. Ohno, H. Making Nonmagnetic Semiconductors Ferromagnetic. *Science* **1998**, *281*, 951–956.
2. Zutic, I.; Fabian, J.; Sarma, S. D. Spintronics: Fundamentals and Applications. *Rev. Mod. Phys.* **2004**, *76*, 323–410.
3. Wang, Y.; Huang, Y.; Song, Y.; Zhang, X.; Ma, Y.; Liang, J.; Chen, Y. Room-Temperature Ferromagnetism of Graphene. *Nano Lett.* **2008**, *9*, 220.
4. McCreary, K. M.; Swartz, A. G.; Han, W.; Fabian, J.; Kawakami, R. K. Magnetic Moment Formation in Graphene Detected by Scattering of Pure Spin Currents. *Phys. Rev. Lett.* **2012**, *109*, 186604.
5. Saha, S. K.; Baskey, M.; Majumdar, D. Graphene Quantum Sheets: A New Material for Spintronic Applications. *Adv. Mater.* **2010**, *22*, 5531–5536.
6. Feng, Q.; Tang, N.; Liu, F.; Cao, Q.; Zheng, W.; Ren, W.; Wan, X.; Du, Y. Obtaining High Localized Spin Magnetic Moments by Fluorination of Reduced Graphene Oxide. *ACS Nano* **2013**, *7*, 6729–6734.
7. Yazyev, O. V. Emergence of Magnetism in Graphene Materials and Nanostructures. *Rep. Prog. Phys.* **2010**, *73*, 056501.
8. Sepioni, M.; Nair, R. R.; Rablen, S.; Narayanan, J.; Tuna, F.; Winpenny, R.; Geim, A. K.; Grigorieva, I. V. Limits on Intrinsic Magnetism in Graphene. *Phys. Rev. Lett.* **2010**, *105*, 207205.

9. Lehtinen, P.; Foster, A.; Ma, Y.; Krasheninnikov, A.; Nieminen, R. Irradiation-Induced Magnetism in Graphite: A Density Functional Study. *Phys. Rev. Lett.* **2004**, *93*, 187202.
10. Yazyev, O. V.; Lothar, H. Defect-Induced Magnetism in Graphene. *Phys. Rev. B* **2007**, *75*, 125408.
11. Zhang, Y.; Talapatra, S.; Kar, S.; Vajtai, R.; Nayak, S. K.; Ajayan, P. M. First-Principles Study of Defect-Induced Magnetism in Carbon. *Phys. Rev. Lett.* **2007**, *99*, 107201.
12. Artyukhov, V. I.; Chernozatonskii, L. A. Vacancy-Patterned Graphene: A Meta-Material for Spintronics. *Phys. Status Solidi B* **2009**, *246*, 2534–2539.
13. Wu, M.; Wu, X.; Gao, Y.; Zeng, X. C. Patterned Hydrogenation of Graphene: Magnetic Quantum Dot Array. *J. Phys. Chem. C* **2009**, *114*, 139–142.
14. Zhou, J.; Wang, Q.; Sun, Q.; Chen, X. S.; Kawazoe, Y.; Jena, P. Ferromagnetism in Semihydrogenated Graphene Sheet. *Nano Lett.* **2009**, *9*, 3867–3870.
15. Lee, H.; Son, Y. W.; Park, N.; Han, S.; Yu, J. Magnetic Ordering at the Edges of Graphitic Fragments: Magnetic Tail Interactions Between the Edge-Localized States. *Phys. Rev. B* **2005**, *72*, 174431.
16. Uchoa, B.; Kotov, V. N.; Peres, N. M. R.; Castro Neto, A. H. Localized Magnetic States in Graphene. *Phys. Rev. Lett.* **2008**, *101*, 026805.
17. Lehtinen, P. O.; Foster, A. S.; Ayuela, A.; Krasheninnikov, A.; Nordlund, K.; Nieminen, R. M. Magnetic Properties and Diffusion of Adatoms on a Graphene Sheet. *Phys. Rev. Lett.* **2003**, *91*, 017202.
18. Kou, L.; Tang, C.; Guo, W.; Chen, C. Tunable Magnetism in Strained Graphene with Topological Line Defect. *ACS Nano* **2011**, *5*, 1012–1017.
19. Fujita, M.; Wakabayashi, K.; Nakada, K.; Kusakabe, K. Peculiar Localized State at Zigzag Graphite Edge. *J. Phys. Soc. Jpn.* **1996**, *7*, 1920–1923.
20. Son, Y. W.; Cohen, M. L.; Louie, S. G. Half-Metallic Graphene Nanoribbons. *Nature* **2006**, *444*, 347–349.
21. Ma, Y.; Dai, Y.; Guo, M.; Huang, B. Graphene-Diamond Interface: Gap Opening and Electronic Spin Injection. *Phys. Rev. B* **2012**, *85*, 235448.
22. Miao, X.; Tongay, S.; Hebard, A. F. Extinction of Ferromagnetism in Highly Ordered Pyrolytic Graphite by Annealing. *Carbon* **2012**, *50*, 1614–1618.
23. Kim, K.; Lee, Z.; Regan, W.; Kisielowski, C.; Crommie, M. F.; Zettl, A. Grain Boundary Mapping in Polycrystalline Graphene. *ACS Nano* **2011**, *5*, 2142.
24. Huang, P. Y.; Ruiz-Vargas, C. S.; van der Zande, A. M.; Whitney, W. S.; Levendorf, M. P.; Kevek, J. W.; Muller, D. A. Grains and Grain Boundaries in Single-Layer Graphene Atomic Patchwork Quilts. *Nature* **2011**, *469*, 389–392.
25. Yu, Q.; Jauregui, L. A.; Wu, W.; Colby, R.; Tian, J.; Su, Z.; Chen, Y. P. Control and Characterization of Individual Grains and Grain Boundaries in Graphene Grown by Chemical Vapour Deposition. *Nat. Mater.* **2011**, *10*, 443–449.
26. An, J.; Voelkl, E.; Suk, J. W.; Li, X.; Magnuson, C. W.; Fu, L.; Ruoff, R. S. Domain (Grain) Boundaries and Evidence of "Twinlike" Structures in Chemically Vapor Deposited Grown Graphene. *ACS Nano* **2011**, *5*, 2433–2439.
27. Liu, Y.; Yakobson, B. I. Cones, Pringles, and Grain Boundary Landscapes in Graphene Topology. *Nano Lett.* **2010**, *10*, 2178–2183.
28. Yazyev, O. V.; Louie, S. G. Electronic Transport in Polycrystalline Graphene. *Nat. Mater.* **2010**, *9*, 806–809.
29. Yazyev, O. V.; Louie, S. G. Topological Defects in Graphene: Dislocations and Grain Boundaries. *Phys. Rev. B* **2010**, *81*, 195420.
30. Banhart, F.; Kotakoski, J.; Krasheninnikov, A. V. Structural Defects in Graphene. *ACS Nano* **2010**, *5*, 26–41.
31. Liu, Y.; Zou, X.; Yakobson, B. I. Dislocations and Grain Boundaries in Two-Dimensional Boron Nitride. *ACS Nano* **2012**, *6*, 7053–7058.
32. Gibb, A. L.; Alem, N.; Chen, J.-H.; Erickson, K. J.; Ciston, J.; Gautam, A.; Linck, M.; Zettl, A. Atomic Resolution Imaging of Grain Boundary Defects in Monolayer Chemical Vapor Deposition-Grown Hexagonal Boron Nitride. *J. Am. Chem. Soc.* **2013**, *135*, 6758–6761.
33. Lu, P.; Wu, X.; Guo, W.; Zeng, X. C. Strain-Dependent Electronic and Magnetic Properties of MoS_2 Monolayer, Bilayer, Nanoribbons and Nanotubes. *Phys. Chem. Chem. Phys.* **2012**, *14*, 13035–13040.
34. Radisavljevic, B.; Radenovic, A.; Brivio, J.; Giacometti, V.; Kis, A. Single-Layer MoS_2 Transistors. *Nat. Nanotechnol.* **2011**, *6*, 147–150.
35. Zhang, Y.; Ye, J.; Matsuhashi, Y.; Iwasa, Y. Ambipolar MoS_2 Thin Flake Transistors. *Nano Lett.* **2012**, *12*, 1136–1140.
36. Radisavljevic, B.; Whitwick, M. B.; Kis, A. Integrated Circuits and Logic Operations Based on Single-Layer MoS_2. *ACS Nano* **2011**, *5*, 9934–9938.
37. Mak, K. F.; Lee, C.; Hone, J.; Shan, J.; Heinz, T. F. Atomically Thin MoS_2: A New Direct-Gap Semiconductor. *Phys. Rev. Lett.* **2010**, *105*, 136805.
38. Chhowalla, M.; Shin, H. S.; Eda, G.; Li, L.-J.; Loh, K. P.; Zhang, H. The Chemistry of Two-Dimensional Layered Transition Metal Dichalcogenide Nanosheets. *Nat. Chem.* **2013**, *5*, 263–275.
39. Feng, J.; Qian, X.; Huang, C. W.; Li, J. Strain-Engineered Artificial Atom as a Broad-Spectrum Solar Energy Funnel. *Nat. Photonics* **2012**, *6*, 866–872.
40. Ma, Y.; Dai, Y.; Guo, M.; Niu, C.; Zhu, Y.; Huang, B. Evidence of the Existence of Magnetism in Pristine VX_2 Monolayers (X = S, Se) and Their Strain-Induced Tunable Magnetic Properties. *ACS Nano* **2012**, *6*, 1695–1701.
41. Zou, X.; Liu, Y.; Yakobson, B. I. Predicting Dislocations and Grain Boundaries in Two-Dimensional Metal-Disulfides from the First Principles. *Nano Lett.* **2012**, *13*, 253–258.
42. van der Zande, A. M.; Huang, P. Y.; Chenet, D. A.; Berkelbach, T. C.; You, Y.; Lee, G. H.; Hone, J. C. Grains and Grain Boundaries in Highly Crystalline Monolayer Molybdenum Disulfide. *Nat. Mater.* **2013**, *12*, 554–561.
43. Najmaei, S.; Liu, Z.; Zhou, W.; Zou, X.; Shi, G.; Lei, S.; Yakobson, B. I.; Idrobo, J. C.; Ajayan, P. M.; Lou, J. Vapor Phase Growth and Grain Boundary Structure of Molybdenum Disulfide Atomic Layers. *Nat. Mater.* **2013**, *12*, 754–759.
44. Zhou, W.; Zou, X.; Najmaei, S.; Liu, Z.; Shi, Y.; Kong, J.; Lou, J.; Ajayan, P. M.; Yakobson, B. I.; Idrobo, J. C. Intrinsic Structural Defects in Monolayer Molybdenum Disulfide. *Nano Lett.* **2013**, *13*, 2615–2622.
45. Zhang, Y.; Zhang, Y.; Ji, Q.; Ju, J.; Yuan, H.; Shi, J.; Gao, T.; Ma, D.; Liu, M.; Chen, Y. *et al.* Controlled Growth of High Quality Monolayer WS2 Layers on Sapphire and Imaging its Grain Boundary. *ACS Nano* **2013**, *7*, 8963−8971.
46. Enyashin, A. N.; Sadan, M. B.; Houben, L.; Seifert, G. Line Defects in Molybdenum Disulfide Layers. *J. Phys. Chem. C* **2013**, *117*, 10842–10848.
47. Seifert, G.; Terrones, H.; Terrones, M.; Jungnickel, G.; Frauenheim, T. Structure and Electronic Properties of MoS_2 Nanotubes. *Phys. Rev. Lett.* **2000**, *85*, 146–149.
48. Yakobson, B. I. Mechanical Relaxation and 'Intramolecular Plasticity' in Carbon Nanotubes. *Appl. Phys. Lett.* **1998**, *72*, 918–920.
49. Li, Y.; Zhou, Z.; Zhang, S.; Chen, Z. MoS_2 Nanoribbons: High Stability and Unusual Electronic and Magnetic Properties. *J. Am. Chem. Soc.* **2008**, *130*, 16739–16744.
50. Gao, D.; Si, M.; Li, J.; Zhang, J.; Zhang, Z.; Yang, Z.; Xue, D. Ferromagnetism in Freestanding MoS_2 Nanosheets. *Nanoscale Res. Lett.* **2013**, *8*, 1–8.
51. Tongay, S.; Varnoosfaderani, S. S.; Appleton, B. R.; Wu, J.; Hebard, A. F. Magnetic Properties of MoS_2: Existence of Ferromagnetism. *Appl. Phys. Lett.* **2012**, *101*, 123105.
52. Le, D.; Rahman, T. S. Joined Edges in MoS_2: Metallic and Half-Metallic Wires. *J. Phys.: Condens. Matter* **2013**, *25*, 312201.
53. Ma, Y.; Dai, Y.; Guo, M.; Niu, C.; Lu, J.; Huang, B. Electronic and Magnetic Properties of Perfect, Vacancy-Doped, and Nonmetal Adsorbed $MoSe_2$, $MoTe_2$ and WS_2 Monolayers. *Phys. Chem. Chem. Phys.* **2011**, *13*, 15546–15553.
54. Hirth, J. P.; Lothe, J. *Theory of Dislocations*, 2nd ed.; Wiley: New York, 1982; p 857.

55. Mahadevan, P.; Zunger, A.; Sarma, D. D. Unusual Directional Dependence of Exchange Energies in GaAs Diluted with Mn: Is the RKKY Description Relevant? *Phys. Rev. Lett.* **2004**, *93*, 177201.
56. Wang, Z. Q.; Zhong, X. Y.; Yu, R.; Cheng, Z. Y.; Zhu, J. Quantitative Experimental Determination of Site-Specific Magnetic Structures by Transmitted Electrons. *Nat. Commun.* **2013**, *4*, 1395.
57. Kresse, G.; Hafner, J. *Ab Initio* Molecular-Dynamics Simulation of the Liquid-Metal-Amorphous-Semiconductor Transition in Germanium. *Phys. Rev. B* **1994**, *49*, 14251–14269.
58. Kresse, G.; Furthmuller, J. Efficient Iterative Schemes for *ab Initio* Total-Energy Calculations Using a Plane-Wave Basis Set. *Phys. Rev. B* **1996**, *54*, 11169–11186.
59. Blochl, P. E. Projector Augmented-Wave Method. *Phys. Rev. B* **1994**, *50*, 17953–17979.
60. Perdew, J. P.; Burke, K.; Ernzerhof, M. Generalized Gradient Approximation Made Simple. *Phys. Rev. Lett.* **1996**, *77*, 3865–3868.
61. Heyd, J.; Scuseria, G. E.; Ernzerhof, M. Hybrid Functionals Based on a Screened Coulomb Potential. *J. Chem. Phys.* **2003**, *118*, 8207–8215.